Progress in Natural Science: Materials International 36 (2026) 76–83

HOSTED BY

Contents lists available at ScienceDirect

Progress in Natural Science: Materials International

journal homepage: www.elsevier.com/locate/pnsmi

Stabilization of 1T MoS_2 via Co/Se Co-doping for high-rate sodium storage

Zhengguang Fu[a,*], Xin Zhang[b], Binghe Chen[c], Yiming Xia[c], Xinhao Wei[c], Ruqiang Yuan[d,**], Jutao Sun[a,***]

[a] School of Polymer Science and Engineering, Qingdao University of Science and Technology, Qingdao, Shandong, 266042, China
[b] College of Mechanical and Electrical Engineering, Qingdao University, Qingdao, Shandong, 266071, China
[c] Qingdao Institute of Bioenergy and Bioprocess Technology, Chinese Academy of Sciences, Qingdao, Shandong, 266101, China
[d] Ministry of Industry and Information Technology Equipment Industry Development Center, Beijing, 100846, China

ARTICLE INFO

Keywords:
Sodium-ion batteries
Co/Se co-doping
1T MoS_2 stabilization
Fast-charging anode
Interfacial chemistry regulation

ABSTRACT

Fast-charging sodium-ion batteries are severely constrained by sluggish Na^+ diffusion, structural instability, and rapid capacity fading in layered anodes, representing a major challenge for high-power energy storage applications. Here, a Co and Se co-doping strategy is implemented on MoS_2 (Co–$MoS_{1.8}Se_{0.2}$/C) to stabilize the metallic 1T-like phase, expand interlayer spacing, and introduce abundant defect sites, generating additional redox-active centers that facilitate rapid and reversible Na^+ insertion and extraction. Cobalt doping serves as a catalytic regulator, promoting uniform SEI formation and enhancing interfacial stability, whereas selenium doping reduces Na^+ diffusion barriers and alleviates strain induced by volumetric changes. A conductive carbon framework supports the nanosheet structure, prevents restacking, and buffers mechanical stress, ensuring structural integrity during extreme-rate cycling. The Co–$MoS_{1.8}Se_{0.2}$/C electrode achieves a reversible capacity of 250 mAh g^{-1} at 20 A g^{-1}, corresponding to full charge/discharge in approximately 15 s, and maintains long-term cycling stability over 1400 cycles at 5 A g^{-1}. Structural analyses reveal partial electron transfer from Co and Se to Mo upon intercalation, triggering reorganization of Mo 4d orbitals and inducing a spontaneous 2H-to-1T phase transition, which enhances electrical conductivity. Reversible layered-to-metallic transformation occurs alongside the formation of a stable SEI layer, further promoting electrochemical kinetics and interfacial stability. The synergistic integration of dual-element doping and carbon framework design significantly improves structural robustness and sodium storage performance.

1. Introduction

The accelerating demand for large-scale energy storage has intensified the search for cost-effective and sustainable alternatives to conventional lithium-ion batteries. Sodium-ion batteries (SIBs) have emerged as a promising candidate due to the natural abundance, low cost, and chemical similarity of sodium relative to lithium [1–3]. However, the larger ionic radius and higher standard redox potential of Na^+ impose intrinsic limitations on the kinetics and structural stability of electrode materials, posing formidable challenges for the development of high-performance anodes [4–6]. Specifically, these characteristics often lead to sluggish Na^+ diffusion, significant volume expansion, and rapid capacity degradation during prolonged cycling. Layered transition metal dichalcogenides (TMDs), particularly molybdenum disulfide (MoS_2) [7–10], have attracted extensive attention as anode materials for SIBs, owing to their high theoretical capacity, two-dimensional layered structure, and tunable interlayer spacing [11–13].

To address the intrinsic drawbacks of MoS_2, extensive efforts have been devoted to structural and compositional engineering strategies aimed at enhancing electrical conductivity, mechanical stability, and sodium storage kinetics [14,15]. One widely adopted approach is nanostructuring, which shortens Na^+ diffusion pathways, increases the active surface area, and provides structural flexibility to accommodate volume fluctuations during cycling. Such features effectively accelerate reaction kinetics and improve reversible capacity [16,17]. Nevertheless, excessive nanostructuring inevitably exposes a large surface area to the electrolyte, leading to pronounced side reactions, low initial coulombic

* Corresponding author.
** Corresponding author.
*** Corresponding author.
E-mail addresses: fuzg@qibebt.ac.cn (Z. Fu), yuanruqiang@eidc.org.cn (R. Yuan), jtsun@qust.edu.cn (J. Sun).

https://doi.org/10.1016/j.pnsc.2025.11.001
Received 12 October 2025; Received in revised form 30 October 2025; Accepted 1 November 2025
Available online 3 February 2026

efficiency, and complex synthesis procedures that hinder large-scale application [18–20]. Beyond structural modifications, compositional engineering through elemental doping provides a powerful route to improve intrinsic conductivity, create additional active sites, and stabilize the layered framework. MoS_2 exhibits polymorphism, mainly in the semiconducting 2H phase and the metallic 1T phase [7,12,16]. The 1T phase offers higher electrical conductivity and more favorable Na^+ intercalation channels, which accelerate charge transfer and enhance reversible capacity. However, 1T MoS_2 is metastable under ambient conditions, prone to partial reversion to the 2H phase, and susceptible to lattice distortions or defect formation. Such instability can result in rapid capacity fading and poor cycling performance. Direct synthesis of 1T MoS_2 often yields heterogeneous phase distributions, further compromising structural integrity. Elemental doping can facilitate the 2H → 1T phase transition while stabilizing the 1T structure. Cationic dopants donate electrons to the lattice, lowering the formation energy of the 1T phase, whereas anionic dopants expand interlayer spacing and introduce additional active sites, promoting Na^+ diffusion and accommodating volumetric changes [21,22]. Conventional single-element doping, however, is limited by potential lattice distortion, phase segregation, or defect clustering, which may undermine long-term cycling stability. Inspired by high-entropy material concepts, dual cation–anion and multielement co-doping strategies have recently emerged as a promising pathway [23]. By leveraging synergistic interactions among dopants, these approaches can simultaneously optimize electronic states, interlayer spacing, and structural robustness, overcoming the intrinsic constraints of single-element doping [24,25]. Despite progress in doping strategies, achieving rational dual- or multi-element doping of MoS_2 remains formidable, due to the need for targeted dopant selection, spatially uniform incorporation, and coordinated electronic effects that prevent structural degradation.

In this study, Co and Se co-doped MoS_2 nanosheets were anchored on carbon to achieve a synergistic integration of electronic modulation and structural stabilization for sodium storage (Co–$MoS_{1.8}Se_{0.2}$/C). Cobalt doping, as a cationic modulation, facilitates the stabilization of a metallic 1T-like phase and introduces additional redox-active sites, thereby enhancing charge-transfer kinetics. Meanwhile, selenium doping, as an anionic regulation, effectively enlarges the interlayer spacing and reduces Na^+ diffusion barriers, which accelerates ion transport and mitigates the strain associated with volume change. In parallel, the conductive N,S co-doped carbon framework provides a robust network that suppresses nanosheet restacking, buffers structural stress, and offers heteroatom-derived active sites to stabilize the solid electrolyte interphase. Benefiting from the cooperative effect of dual-element doping and carbon matrix support, the composite simultaneously achieves improved electrical conductivity, stabilized interlayer channels for fast and reversible Na^+ insertion/extraction, and abundant active defect/edge sites that contribute to high capacity and prolonged

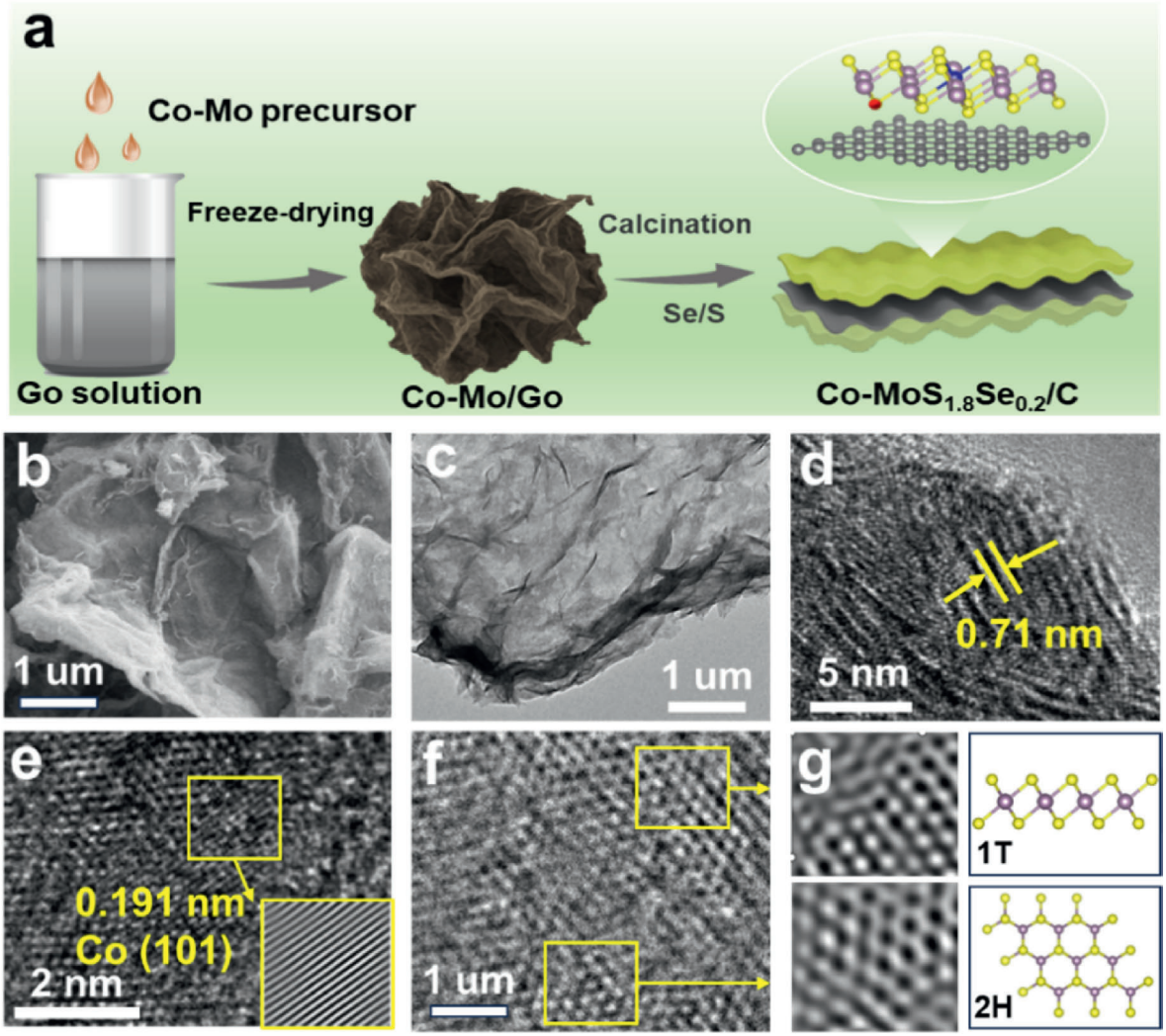

Fig. 1. (a) Schematic illustration of the synthetic process. (b) SEM image. (c) TEM image. (d–f) HRTEM image. (g) Corresponding FFT pattern, and schematic diagram of 1T/2H structure.

durability. Owing to structural and compositional advantages, the optimized Co–$MoS_{1.8}Se_{0.2}$/C electrode delivers a high reversible capacity of 450 mAh g^{-1} at 0.2 A g^{-1}. In addition, exceptional fast-charging performance is achieved, reaching 250 mAh g^{-1} at an ultra-high current density of 20 A g^{-1}, corresponding to full charge/discharge in approximately 15 s. Furthermore, long-term cycling tests demonstrate retention of 85 % of the initial capacity over 1400 cycles at 5 A g^{-1}, with an initial coulombic efficiency of ~98 %. Overall, these results illustrate the effectiveness of Co–$MoS_{1.8}Se_{0.2}$/C for high-power and durable sodium-ion energy storage applications.

2. Results and discussion

The Co–$MoS_{1.8}Se_{0.2}$/C composite was successfully synthesized through a freeze-drying–calcination strategy, as illustrated in Fig. 1a. Initially, the Co–Mo precursor was uniformly dispersed in a graphene oxide (GO) solution, followed by freeze-drying to obtain a three-dimensional Co–Mo/GO aerogel. Subsequent calcination under a mixed S/Se atmosphere facilitated the in situ growth of Co and Se co-doped MoS_2 nanosheets anchored on carbon sheet, forming a hierarchical architecture with intimate interfacial contact. This synthetic route not only enables homogeneous distribution of dopants but also ensures the integration of conductive carbon with the active MoS_2 phase, thereby providing structural robustness and enhanced electron/ion transport pathways. The morphology of the obtained Co–$MoS_{1.8}Se_{0.2}$/C was examined by scanning electron microscopy (SEM) and transmission electron microscopy (TEM). As shown in Fig. 1b, the Co–$MoS_{1.8}Se_{0.2}$/C composite displays wrinkled nanosheets with loose stacking, while the TEM image in Fig. 1c further confirms the ultrathin and transparent nature of these nanosheets, suggesting the successful formation of a two-dimensional layered structure with uniform dispersion on the carbon matrix. Such a porous, three-dimensional network is expected to facilitate electrolyte infiltration and buffer mechanical stress during repeated sodiation/desodiation cycles. High-resolution TEM (HRTEM) images (Fig. 1d) reveal clear lattice fringes with an interplanar spacing of 0.71 nm, corresponding to the expanded (002) plane of MoS_2. The enlarged interlayer distance, induced by Se incorporation, provides more accessible channels for Na^+ intercalation and improves ion transport kinetics. In contrast, SEM analysis (Fig. S1a) shows that the MoS_2/C sample exhibits nanosheets with a morphology largely similar to that of Co–$MoS_{1.8}Se_{0.2}$/C, while TEM characterization (Fig. S1b) reveals a smaller interplanar spacing of 0.62 nm [26,27], corresponding to the (002) plane of MoS_2. In addition, distinct lattice fringes with a spacing of 0.191 nm can be assigned to the (101) plane of metallic Co (Fig. 1e), confirming the successful introduction of cobalt species into the composite. Further atomic-resolution TEM observations (Fig. 1f–g) demonstrate the coexistence of both 1T- and 2H-MoS_2 phases, consistent with the simulated structural models. Notably, abundant lattice distortions and defect sites are observed, which can be attributed to Se incorporation. These defect features not only increase the number of active sites for Na^+ storage but also promote charge redistribution within the MoS_2 framework.

The crystalline structures of the samples were investigated by X-ray diffraction (XRD), as shown in Fig. 2a. Both Co–MoS_2/C and Co–$MoS_{1.8}Se_{0.2}$/C display broad and weak diffraction peaks, indicative of the poor crystallinity of the MoS_2 phase. 14.4°, 32.7°, 39.6°, and 56.4° can be indexed to the (002), (100), (103), and (110) planes of 2H-MoS_2 (JCPDS No. 37–1492), respectively. No distinct diffraction peaks corresponding to cobalt selenide phases are observed, which suggests that the Co and Se dopants are homogeneously incorporated into the MoS_2 lattice without forming secondary crystalline phases. Notably, the (002) reflection of Co–$MoS_{1.8}Se_{0.2}$/C shifts to a lower angle compared to that of MoS_2, corresponding to an enlarged interlayer spacing caused by Se substitution. The expanded interlayer spacing is expected to facilitate Na^+ intercalation and improve diffusion kinetics during electrochemical cycling. To further elucidate the phase structures, Raman spectroscopy was conducted (Fig. 2b). Both Co–MoS_2/C and Co–$MoS_{1.8}Se_{0.2}$/C exhibit the characteristic E^1_{2g} and A_{1g} vibrational modes of MoS_2. In addition, several additional peaks at 144.3 cm^{-1} (J_1), 235.8 cm^{-1} (J_2), 278.9 cm^{-1} (E_{1g}), and 335.8 cm^{-1} (J_3) are observed, which are characteristic fingerprints of the metallic 1T-MoS_2 phase [28–30]. The coexistence of both 2H and 1T phases indicates that Co/Se dual doping promotes a partial 2H → 1T transition, providing enhanced electrical conductivity and more favorable ion diffusion channels. X-ray

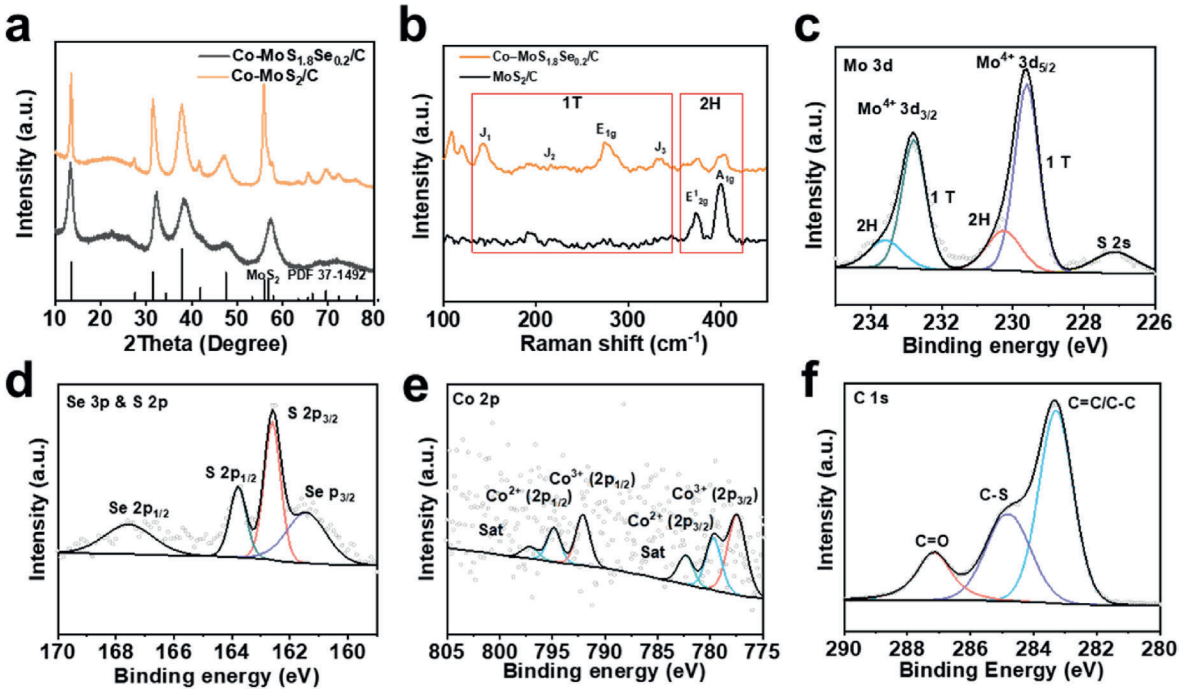

Fig. 2. (a) XRD patterns of Co–MoS_2/C and Co–$MoS_{1.8}Se_{0.2}$/C. (b) Raman spectra of MoS_2/C and Co–$MoS_{1.8}Se_{0.2}$/C. (c–f) XPS spectra of Co–$MoS_{1.8}Se_{0.2}$/C: (c) Mo 3d, (d) Se 3p and S 2p, (e) Co 2p, and (f) C 1s.

photoelectron spectroscopy (XPS) was employed to probe the chemical states and elemental composition of Co–$MoS_{1.8}Se_{0.2}$/C. The high-resolution Mo 3d spectrum (Fig. 2c) can be deconvoluted into peaks at 232.8 eV (Mo $3d_{3/2}$) and 229.7 eV (Mo $3d_{5/2}$), corresponding to 1T-MoS_2, along with peaks at 233.8 eV (Mo $3d_{3/2}$) and 230.4 eV (Mo $3d_{5/2}$), assigned to 2H-MoS_2. This confirms the coexistence of both phases, consistent with Raman results. The S 2p spectrum (Fig. 2d) shows peaks at 163.9 eV and 162.8 eV, slightly shifted toward lower binding energies compared to pristine MoS_2, which can be ascribed to electronic interactions arising from Se incorporation. The presence of Se is further verified by the Se 3p spectrum with peaks at 161.8 and 166.7 eV, as well as the Se 3d spectrum (Fig. S2) at 54.6 and 55.4 eV, confirming successful doping of Se into the MoS_2 framework. In contrast, the MoS_2/C sample exhibits only the characteristic Mo $3d_{3/2}$ and Mo $3d_{5/2}$ peaks of 2H-MoS_2, with no detectable signals corresponding to the 1T phase (Fig. S3). The S 2p spectrum displays solely the conventional S $2p_{3/2}$ and S $2p_{1/2}$ peaks, suggesting the absence of Se-induced electronic interactions (Fig. S3). The high-resolution Co 2p spectrum (Fig. 2e) further confirms the successful incorporation of cobalt species into the composite. The Co $2p_{3/2}$ region can be deconvoluted into two main peaks at 777.5 eV and 780 eV, which are attributed to Co^{3+} and Co^{2+}, respectively. Similarly, the Co $2p_{1/2}$ region shows peaks at 792.2 eV (Co^{3+}) and 795 eV (Co^{2+}). The high-resolution C 1s spectrum (Fig. 2f) can be deconvoluted into three peaks centered at 283.2 eV, 284.8 eV, and 287.1 eV, which are assigned to C–C/C=C, C–S, and C=O bonding configurations, respectively. The clear presence of the C–S bonding signal demonstrates the successful incorporation of sulfur into the carbon framework.

The CV curves of the Co–$MoS_{1.8}Se_{0.2}$/C electrode, shown in Fig. 3a, were measured within a voltage window of 0.01–3 V at a scan rate of 0.1 mV s^{-1}. In the first cathodic cycle, an irreversible peak at 0.85 V can be ascribed to Na^+ insertion, while the peak at 0.2 V corresponds primarily to the conversion of MoS_2 to Mo and Na_2S. During the anodic sweep, the main peak at 1.75 V is associated with Na^+ extraction and the reversible reaction of Mo with Na_2S. From the second cycle onward, the CV curves largely overlap, indicating good electrochemical reversibility. In comparison, the MoS_2/C electrode (Fig. 3b) exhibits three cathodic peaks at 0.9, 0.7, and 0.2 V in the first cycle. The 0.9 V peak corresponds to Na^+ insertion, the 0.7 V peak is attributed to SEI formation, and the 0.2 V peak corresponds to the conversion reaction. Notably, the SEI-related peak is not clearly observed in the Co–$MoS_{1.8}Se_{0.2}$/C electrode, suggesting that a relatively thin SEI forms rapidly during the first cycle. This behavior can be attributed to the interfacial catalytic effect of Co, which facilitates faster charge transfer and promotes stable SEI formation. The initial charge–discharge profiles of Co–$MoS_{1.8}Se_{0.2}$/C and MoS_2/C electrodes were evaluated to investigate their sodium storage behavior. As shown in Fig. 3d, the Co–$MoS_{1.8}Se_{0.2}$/C electrode delivers an initial discharge capacity of 570 mAh g^{-1} and a charge capacity of 480 mAh g^{-1}, corresponding to an initial coulombic efficiency (ICE) of approximately 84 %. In comparison, the MoS_2/C electrode exhibits an initial discharge capacity of 545 mAh g^{-1} and a charge capacity of 440 mAh g^{-1}, resulting in a lower ICE of about 80 % (Fig. 3e). The higher ICE of Co–$MoS_{1.8}Se_{0.2}$/C can be attributed to the synergistic effect of Co and Se co-doping, which

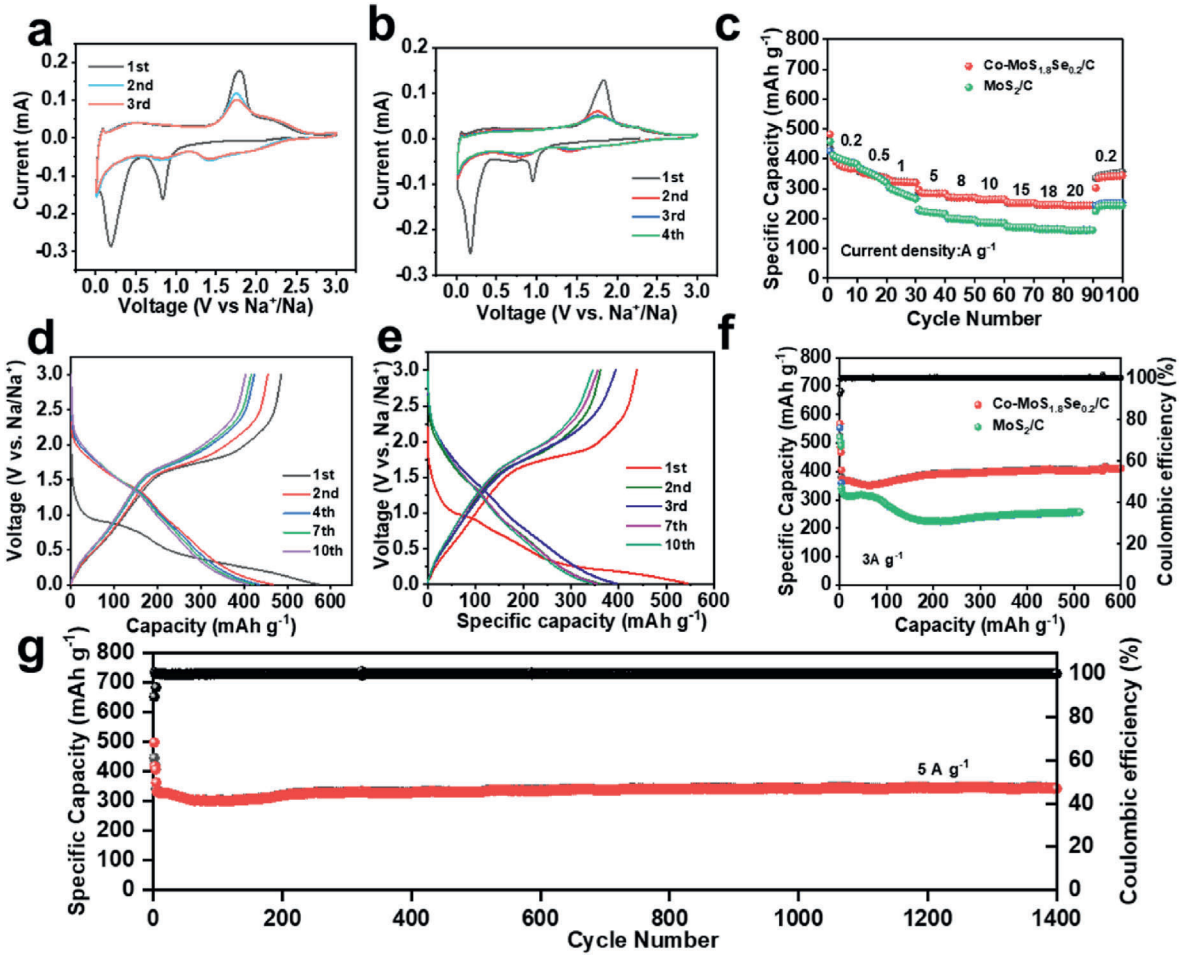

Fig. 3. (a) CV curves of Co–$MoS_{1.8}Se_{0.2}$/C. (b) CV curves of MoS_2/C. (c) Rate performance of Co–$MoS_{1.8}Se_{0.2}$/C and MoS_2/C. (d) Charge–discharge curves of Co–$MoS_{1.8}Se_{0.2}$/C. (e) Charge–discharge curves of MoS_2/C. (f) Cycling performance of Co–$MoS_{1.8}Se_{0.2}$/C and MoS_2/C. (g) Long-term cycling of Co–$MoS_{1.8}Se_{0.2}$/C.

optimizes electronic structure, facilitates Na^+ insertion/extraction, and stabilizes the electrode–electrolyte interface. Compared with undoped MoS_2/C, the improvement in initial Coulombic efficiency (ICE) of the Co–$MoS_{1.8}Se_{0.2}$/C composite is mainly attributed to the introduction of Co. Co doping induces a partial 2H→1T phase transition in MoS_2, which reduces the diffusion barrier for Na^+ at the electrode surface and facilitates more efficient sodium insertion/extraction. In addition, Co can catalyze the decomposition of the electrolyte, promoting the rapid formation of a stable SEI layer during the first cycle. In subsequent cycles, the coulombic efficiency of Co–$MoS_{1.8}Se_{0.2}$/C rapidly increases to 98 % from the second cycle onward and remains close to 100 % during prolonged cycling, indicating highly reversible sodium storage and effective suppression of parasitic side reactions. In contrast, the MoS_2/C electrode exhibits a slower rise in coulombic efficiency during the initial cycles and requires more cycles to stabilize near 100 %, suggesting relatively sluggish interfacial kinetics and less stable SEI formation. The rate performance of Co–$MoS_{1.8}Se_{0.2}$/C and MoS_2/C electrodes was further evaluated under current densities ranging from 0.2 to 20 A g^{-1} (Fig. 3c). The Co–$MoS_{1.8}Se_{0.2}$/C electrode delivers reversible capacities of approximately 300 mAh g^{-1} at 5 A g^{-1}, 280 mAh g^{-1} at 8 A g^{-1}, 260 mAh g^{-1} at 10 A g^{-1}, 250 mAh g^{-1} at 15 A g^{-1}, 245 mAh g^{-1} at 18 A g^{-1}, and 240 mAh g^{-1} at 20 A g^{-1}, demonstrating outstanding rate capability with only a slight capacity decay even at ultrahigh current densities. Remarkably, at 20 A g^{-1}, a full charge/discharge process can be completed within ~15 s, highlighting the ultrafast sodium storage kinetics of the dual-doped composite. More importantly, when the current density is returned to 0.2 A g^{-1}, the reversible capacity recovers to ~350 mAh g^{-1}, indicating excellent structural robustness and superior reversibility under extreme conditions. In contrast, the MoS_2/C electrode exhibits significantly lower rate performance, with rapid capacity fading at elevated current densities. At 20 A g^{-1}, the reversible capacity decreases to ~170 mAh g^{-1}, and the recovered capacity after returning to 0.2 A g^{-1} remains notably lower than the initial value, suggesting irreversible structural degradation and unstable electrode–electrolyte interface. The cycling performance of Co–$MoS_{1.8}Se_{0.2}$/C and MoS_2/C electrodes was evaluated at a current density of 3 A g^{-1} (Fig. 3f). The Co–$MoS_{1.8}Se_{0.2}$/C electrode delivers a stable reversible capacity of ~400 mAh g^{-1}, which is well maintained over 600 cycles without noticeable capacity fading, demonstrating remarkable cycling durability. In contrast, the MoS_2/C electrode exhibits rapid capacity decay, with the reversible capacity dropping to ~210 mAh g^{-1} after 100 cycles. Furthermore, continuous cycling results in severe degradation, eventually leading to cell failure and short circuit after ~500 cycles. To further evaluate durability under high-rate conditions, long-term cycling of the Co–$MoS_{1.8}Se_{0.2}$/C electrode was conducted at a current density of 5 A g^{-1} (Fig. 3g). The electrode maintains a highly stable reversible capacity of ~300 mAh g^{-1} over 1400 cycles without observable capacity decay, demonstrating outstanding structural robustness and electrochemical reversibility. In addition, the coulombic efficiency remains close to 100 % throughout the entire cycling process, confirming efficient suppression of side reactions and excellent electrode–electrolyte interfacial stability.

The electrochemical kinetics of Co–$MoS_{1.8}Se_{0.2}$/C were systematically evaluated by cyclic voltammetry (CV) at different scan rates

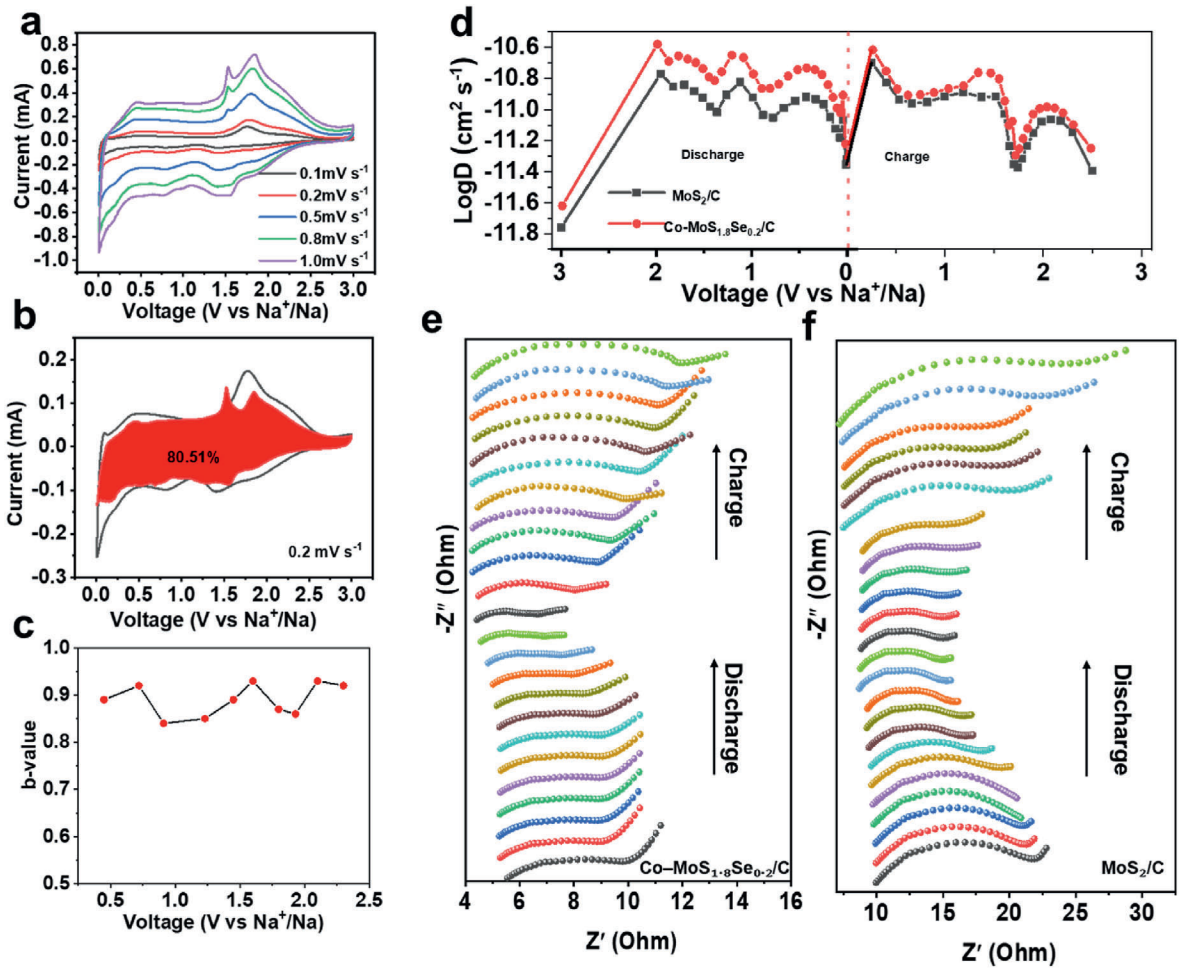

Fig. 4. (a) CV curves of Co–$MoS_{1.8}Se_{0.2}$/C at different scan rates (0.1–1 mV s^{-1}). (b) Pseudocapacitive contribution at 0.2 mV s^{-1}. (c) b values. (d) Na^+ diffusion coefficients calculated from GITT. (e–f) In situ EIS of Co–$MoS_{1.8}Se_{0.2}$/C and MoS_2/C.

(0.1–1 mV s^{-1}) (Fig. 4a). The relationship between peak current (i) and scan rate (v) follows the power-law equation:

$$i = av^b$$

where *a* is a constant and *b* reflects the charge storage mechanism. A b value of 0.5 indicates a semi-infinite diffusion-controlled process dominated by ion intercalation, whereas a b value of 1.0 corresponds to a capacitive process governed by surface-controlled reactions. The calculated b values for both anodic and cathodic peaks are approximately 0.85 across the entire potential window (Fig. 4c), suggesting that the sodium storage in Co–$MoS_{1.8}Se_{0.2}$/C is dominated by pseudocapacitive behavior with partial contribution from diffusion-controlled intercalation. To further distinguish between capacitive and diffusion contributions, the current response at a fixed potential can be expressed as:

$$i(V) = k_1v + k_2v^{1/2}$$

where k_1v corresponds to the surface-controlled (capacitive) contribution and $k_2v^{1}\square^{2}$ represents the diffusion-controlled contribution [31,32]. Quantitative analysis at 0.2 mV s^{-1} reveals that pseudocapacitive processes contribute ~80 % of the total capacity (Fig. 4b). This large pseudocapacitive fraction confirms that the Co–$MoS_{1.8}Se_{0.2}$/C electrode enables rapid charge storage via surface redox reactions and interfacial adsorption, which accounts for its excellent rate capability and high reversibility under ultrafast cycling. The Na^+ diffusion kinetics of Co–$MoS_{1.8}Se_{0.2}$/C and MoS_2/C electrodes were further investigated by galvanostatic intermittent titration technique (GITT). The Na^+ diffusion coefficient (D_{Na}^{+}) was calculated according to Fick's second law (Fig. S4).

As shown in Fig. 4d, the Na^+ diffusion coefficient of Co–$MoS_{1.8}Se_{0.2}$/C during both sodiation and desodiation processes remains in the range of 10^{-10}–10^{-11} cm^2 s^{-1}, which is higher than that of MoS_2/C across the entire voltage window. The superior $D_{Na}{}^{+}$ values indicate faster ion transport kinetics enabled by Co and Se co-doping. Specifically, the enlarged interlayer spacing induced by Se substitution lowers the diffusion barrier, while Co incorporation enhances electronic conductivity and facilitates charge transfer. The interfacial charge-transfer behavior of Co–$MoS_{1.8}Se_{0.2}$/C and MoS_2/C electrodes was further evaluated by in-situ electrochemical impedance spectroscopy (EIS) during the sodiation/desodiation process (Fig. 4e–f). The Nyquist plots of both electrodes consist of a depressed semicircle in the high-to-medium frequency region, associated with charge-transfer resistance (*Rct*), and a straight line in the low-frequency region, corresponding to the Warburg impedance of Na^+ diffusion. During the discharge process, the Rct of Co–$MoS_{1.8}Se_{0.2}$/C gradually decreases, reflecting progressively enhanced charge transfer. This behavior is mainly attributed to

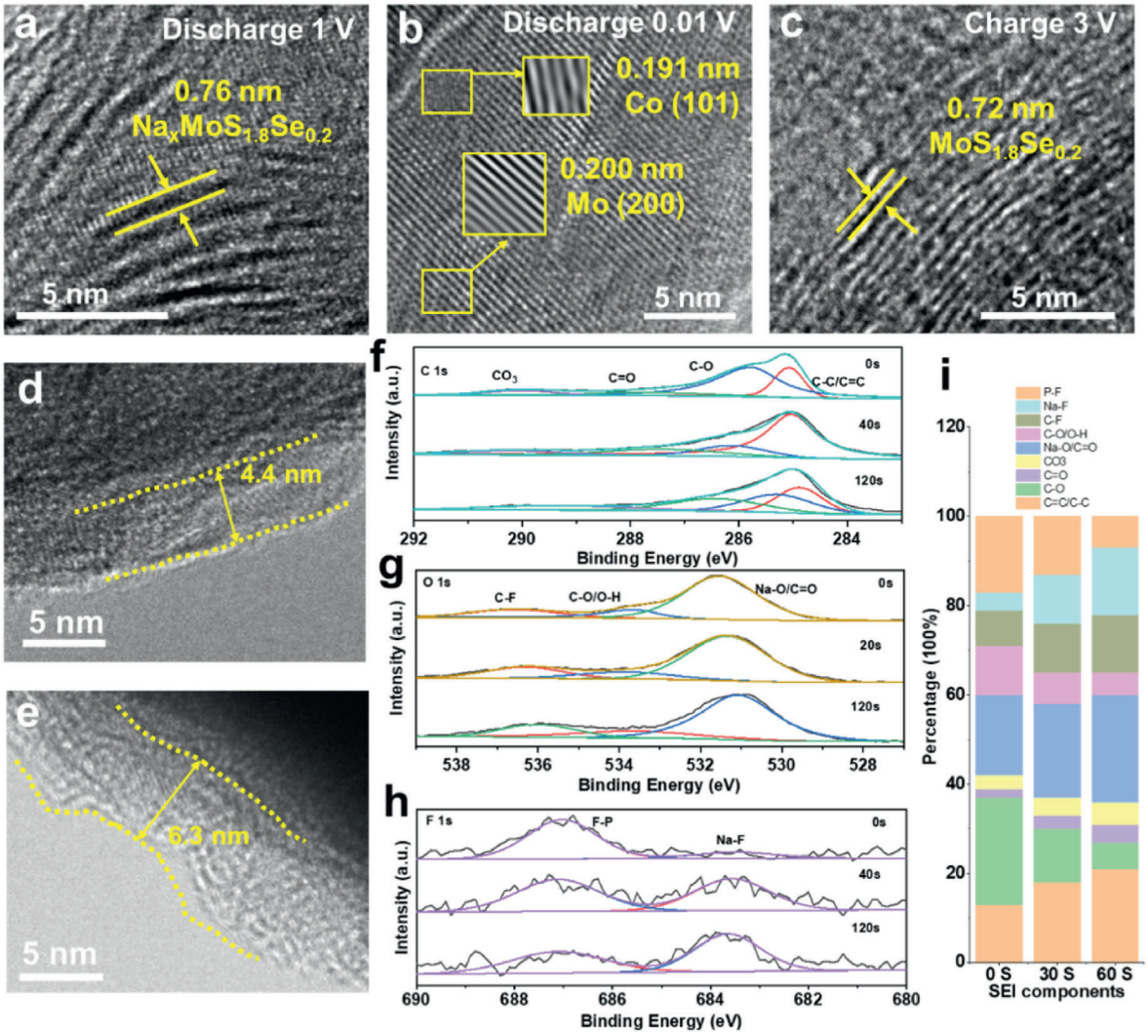

Fig. 5. (a–c) Co–$MoS_{1.8}Se_{0.2}$/C at different states: discharge 1 V, discharge 0.01 V, and charge 3 V. (d) SEI thickness of Co–$MoS_{1.8}Se_{0.2}$/C after cycling. (e) SEI thickness of MoS_2/C after cycling. (f–i) In-depth XPS analysis of Co–$MoS_{1.8}Se_{0.2}$/C: (f) C 1s, (g) O 1s, (h) F 1s, and (i) Relative proportions of different functional groups.

the in-situ formation of Mo-related conductive species during sodiation, which significantly improves electronic conductivity, while the expanded interlayer spacing and defect sites introduced by Co/Se co-doping further facilitate Na^+ insertion. In the subsequent charge process, *Rct* increases slightly, which may be associated with partial structural relaxation and reconstruction of the electrode–electrolyte interface. Importantly, the overall *Rct* values of Co–$MoS_{1.8}Se_{0.2}$/C remain significantly lower than those of MoS_2/C throughout cycling, suggesting superior electronic conductivity and interfacial stability.

HRTEM was employed to probe the structural evolution of Co–$MoS_{1.8}Se_{0.2}$/C during charge–discharge processes. At 1 V discharge (Fig. 5a), lattice fringes of 0.76 nm indicate that the layered structure remains intact, corresponding to the partially sodiated phase Na_x-$MoS_{1.8}Se_{0.2}$, with no significant conversion reaction occurring. Upon full discharge to 0.01 V (Fig. 5b), lattice fringes of 0.200 nm and 0.191 nm were observed, corresponding to the (200) plane of metallic Mo and the (101) plane of Co, evidencing the completion of conversion reactions. After charging to 3 V (Fig. 5c), the lattice spacing contracts to 0.72 nm, suggesting partial restoration of the layered structure. These observations indicate that Co–$MoS_{1.8}Se_{0.2}$/C undergoes reversible structural evolution, where the initial layered framework accommodates Na^+ insertion/extraction Post-cycling TEM analysis was performed to examine the SEI layer on Co–$MoS_{1.8}Se_{0.2}$/C and MoS_2/C electrodes. For Co–$MoS_{1.8}Se_{0.2}$/C, a uniform SEI layer with a thickness of ~4.4 nm was observed (Fig. 5d), indicating stable interfacial formation during repeated sodiation/desodiation. In contrast, MoS_2/C exhibited a thicker (~6.3 nm) and uneven SEI layer (Fig. 5e), suggesting uncontrolled interfacial growth and possible aggregation of decomposition products. TEM analyses were conducted on the Co–$MoS_{1.8}Se_{0.2}$/C electrodes after 100 charge-discharge cycles at 3 A g^{-1} (Fig. S5). The TEM images show that the nanosheet morphology is largely preserved and confirm that the MoS_2 lattice fringes remain clearly visible. Depth-resolved XPS measurements were carried out to elucidate the chemical composition and depth distribution of the SEI film formed on Co–$MoS_{1.8}Se_{0.2}$/C after cycling. The C 1s spectra (Fig. 5f) show three major peaks at 284.8, 285.8V and 288.1 eV, which can be assigned to C–C/C=C, C–O, and C=O species, respectively. At the outermost SEI surface, strong contributions from oxygenated carbon species (C=O) are observed, indicative of organic sodium carbonate and polymeric byproducts generated from electrolyte decomposition. With increasing etching depth, the relative intensity of C=O decreases, whereas the contribution of C–C/C=C becomes more pronounced, suggesting that organic species dominate the outer SEI while carbonaceous residues and inorganic phases are enriched in the inner region. Fig. 5g shows the depth-dependent O 1s spectra of the cycled Co–$MoS_{1.8}Se_{0.2}$/C electrode at etching times of 0 s, 20 s, and 120 s. Three distinct components can be identified: the high-binding-energy peak at ~536–537 eV corresponds to C–F species, the intermediate peak at ~533–534 eV is assigned to C–O/O–H groups, and the lower-binding-energy peak at ~531–532 eV is attributed to Na–O/C=O species [33]. At the surface (0 s), the O 1s spectrum is dominated by C–O/O–H contributions, accompanied by noticeable C–F signals, indicating the prevalence of organic/polymeric decomposition products and fluorinated organic species in the outer SEI. With increasing etching depth (20 s and 120 s), the relative intensity of the C–O/O–H and C–F components gradually decreases, while the Na–O/C=O contribution becomes increasingly prominent and shifts slightly toward lower binding energy, suggesting the enrichment of inorganic Na-containing oxides and carbonates in the inner SEI [34,35]. The F 1s spectra (Fig. 5h) present a primary peak centered at ~683.8 eV, attributed to NaF, together with a higher binding-energy component at ~687.0 eV that can be assigned to sodium fluorophosphates ($Na_xPF_yO_z$) [36,37]. The NaF intensity becomes increasingly prominent with etching depth, demonstrating that inorganic NaF is mainly distributed in the inner SEI layer, serving as a passivation component with high mechanical and chemical stability [[38,39]{Han, 2025 #940}]. The depth-dependent distribution of functional groups is summarized in Fig. 5i. Taken together, the depth-dependent XPS results reveal a bilayered SEI structure on Co–$MoS_{1.8}Se_{0.2}$/C, in which organic carbonates and polymeric species dominate the outer surface, while the inner region is enriched with inorganic components such as NaF and metal oxides. Such a graded SEI architecture is expected to provide both interfacial stability and fast Na^+ transport, thereby accounting for the superior cycling durability of the composite electrode.

3. Conclusion

In summary, A Co and Se co-doped MoS_2–carbon composite was developed as a high-performance anode for sodium-ion batteries. Specifically, Co doping serves as a cationic modulator that stabilizes the metallic 1T-like phase and simultaneously facilitates the rapid formation of a uniform SEI layer, thereby enhancing interfacial stability during cycling. In parallel, Se doping acts as an anionic regulator, effectively enlarging the interlayer spacing and reducing Na^+ diffusion barriers, which promotes faster ion transport and mitigates strain induced by volume changes. Moreover, the incorporation of doping-induced defect sites introduces abundant redox-active centers, further contributing to reversible sodium storage. At the same time, the carbon matrix provides a conductive and robust framework that prevents nanosheet restacking, buffers structural stress, and supports the overall electrode architecture, ensuring structural integrity during prolonged cycling. As a result, the Co–$MoS_{1.8}Se_{0.2}$/C electrode delivers a high reversible capacity of 450 mAh g^{-1} at 0.2 A g^{-1}, maintains excellent rate performance with 250 mAh g^{-1} at 20 A g^{-1}, and exhibits long-term cycling stability over 1400 cycles at a high current density of 5 A g^{-1}. Taken together, the combination of dual-element doping and carbon matrix integration not only optimizes the structural and interfacial properties of the electrode but also enhances electrochemical kinetics and durability. These findings offer valuable insights into the rational design of layered TMD anodes and present a practical strategy for advancing sodium-ion batteries toward large-scale, durable, and efficient energy storage applications.

CRediT authorship contribution statement

Zhengguang Fu: Writing – original draft, Methodology, Investigation. **Xin Zhang:** Investigation, Data curation. **Binghe Chen:** Investigation. **Yiming Xia:** Investigation. **Xinhao Wei:** Methodology. **Ruqiang Yuan:** Resources. **Jutao Sun:** Writing – review & editing, Supervision.

Declaration of competing interest

The authors declare that they have no known competing financial interests or personal relationships that could have appeared to influence the work reported in this paper.

Acknowledgements

This work was financially supported by the supported by Shandong Provincial Natural Science Foundation (ZR2024MB108).

Appendix A. Supplementary data

Supplementary data to this article can be found online at https://doi.org/10.1016/j.pnsc.2025.11.001.

References

[1] Z. He, Y. Huang, H. Liu, Z. Geng, Y. Li, S. Li, W. Deng, G. Zou, H. Hou, X. Ji, Anode materials for fast charging sodium-ion batteries, Nano Energy 129 (2004) 109996.
[2] T. Jin, X. Ji, P.F. Wang, K. Zhu, J. Zhang, L. Cao, L. Chen, C. Cui, T. Deng, S. Liu, N. Piao, Y. Liu, C. Shen, K. Xie, L. Jiao, C. Wang, High-energy aqueous sodium-ion batteries, Angew. Chem. Int. Ed. 60 (21) (2021) 11943–11948.

[3] P.K. Nayak, L. Yang, W. Brehm, P. Adelhelm, From lithium-ion to sodium-ion batteries: advantages, challenges, and surprises, Angew. Chem. Int. Ed. 57 (1) (2017) 102–120.
[4] S. Qiao, Q. Zhou, M. Ma, H.K. Liu, S.X. Dou, S. Chong, Advanced anode materials for rechargeable sodium-ion batteries, ACS Nano 17 (12) (2023) 11220–11252.
[5] H. Zhang, I. Hasa, S. Passerini, Sodium-ion batteries: beyond insertion for Na-Ion batteries: nanostructured alloying and conversion anode materials, Adv. Energy Mater. 8 (17) (2018) 1870082.
[6] W. Zhang, F. Zhang, F. Ming, H.N. Alshareef, Sodium-ion battery anodes: status and future trends, EnergyChem 1 (2) (2019) 100012.
[7] H. He, X. Li, D. Huang, J. Luan, S. Liu, W.K. Pang, D. Sun, Y. Tang, W. Zhou, L. He, C. Zhang, H. Wang, Z. Guo, Electron-injection-engineering induced phase transition toward stabilized 1T-MoS_2 with extraordinary sodium storage performance, ACS Nano 15 (5) (2021) 8896–8906.
[8] Y. Zhang, J. Li, X. Li, L. Shan, W. Zhao, J. Wang, Q. Gao, Z. Cai, C. Zhou, B. Han, K. Amine, R. Sun, Electron configuration modulation induced stabilized 1T-MoS_2 for enhanced sodium ion storage, Nano Lett. 24 (11) (2024) 3331–3338.
[9] Y. Zhang, J. Wang, L. Shan, B. Han, Q. Gao, Z. Cai, C. Zhou, X. Tian, R. Sun, L. Mai, Electron modulated and phosphate radical stabilized 1T-Rich MoS_2 for ultra-fast-charged sodium ion storage, Adv. Energy Mater. 14 (9) (2023).
[10] C. Zhu, X. Mu, P.A. van Aken, Y. Yu, J. Maier, Single-layered ultrasmall nanoplates of MoS2 embedded in carbon nanofibers with excellent electrochemical performance for lithium and sodium storage, Angew. Chem. Int. Ed. 53 (8) (2014) 2152–2156.
[11] Z. Li, M. Han, J. Wang, L. Zhang, P. Yu, Q. Li, X. Bai, J. Yu, Superparamagnetic Fe conversion induces MoS2 fast ion transport in wide-temperature-range sodium-ion batteries, Adv. Funct. Mater. 34 (41) (2024) 2404263.
[12] S. Tian, W. Chen, R. Wang, C. Qin, Z.J. Jiang, Z. Jiang, Ar/NH_3 radio-frequency plasma etching and n-doping to stabilize metallic phase 1T-MoS_2 for fast and durable sodium-ion storage, Adv. Funct. Mater. 34 (46) (2024) 2408035.
[13] N. Wu, Z. Zhao, R. Hua, X. Wang, Y. Zhang, J. Li, G. Liu, D. Guo, G. Sun, X. Liu, J. Zhang, Pre-doping of dual-functional sodium to weaken fe—s bond and stabilize interfacial chemistry for high-rate reversible sodium storage, Adv. Energy Mater. 14 (30) (2024) 2400371.
[14] F. Yang, S. Wang, J. Guan, L. Shao, X. Shi, J. Cai, Z. Sun, Hierarchical MoS_2–NiS nanosheet-based nanotubes@N-doped carbon coupled with ether-based electrolytes towards high-performance Na-ion batteries, J. Mater. Chem. A 9 (2021) 27072–27083.
[15] H. Chen, T. Song, L. Tang, X. Pu, Z. Li, Q. Xu, H. Liu, Y. Wang, Y. Xia, In-situ growth of vertically aligned MoS_2 nanowalls on reduced graphene oxide enables a large capacity and highly stable anode for sodium ion storage, J. Power Sources 445 (2019) 227271.
[16] J. Sun, Z. Zhang, G. Lian, Y. Li, L. Jing, M. Zhao, D. Cui, Q. Wang, H. Yu, C.-P. Wong, Electron-injection and atomic-interface engineering toward stabilized defected 1T-Rich MoS2 as high rate anode for sodium storage, ACS Nano 16 (8) (2022) 12425–12436.
[17] Y. Tang, G. Li, S. Cui, W. Cui, H. Chong, L. Han, H. Pang, Synergistic effects of confinement structure and local-expanded interlayer spacing in $Fe_2Mo_3O_8$@C@MoS_2 toward high-efficient sodium ion storage, Adv. Funct. Mater. 34 (39) (2024) 2403351.
[18] S. Chen, X. Xu, T. Yang, W. Fan, J. Zhao, Y. Huo, Emerging organic carbonyl small molecules cathode materials in alkali-ion batteries: principles, recent progresses, strategies and prospects, Prog. Nat. Sci. Mater. Int. 35 (1) (2025) 31–50.
[19] Y. Li, P. Huang, C. Cui, X. Ma, L. Chen, Z. Li, L. Li, Y. Tian, Additives strategies to improving cycling stability of li metal batteries by modifying electrode electrolyte interphases, Prog. Nat. Sci. Mater. Int. 34 (2) (2024) 338–344.
[20] C. Lin, L. Ouyang, R. Hu, J. Liu, L. Yang, H. Shao, M. Zhu, Synthesis of amorphous SeP_2/C composite by plasma assisted ball milling for high-performance anode materials of lithium and sodium-ion batteries, Prog. Nat. Sci. Mater. Int. 31 (2) (2021) 567–574.
[21] F. Liu, Y. Zou, X. Tang, L. Mao, D. Du, H. Wang, M. Zhang, Z. Wang, N. Yao, W. Zhao, M. Bai, T. Zhao, Y. Liu, Y. Ma, Phase engineering and alkali cation stabilization for 1T molybdenum dichalcogenides monolayers, Adv. Funct. Mater. 32 (36) (2022) 2204601.
[22] T. Wang, C. Sun, M. Yang, G. Zhao, S. Wang, F. Ma, L. Zhang, Y. Shao, Y. Wu, B. Huang, X. Hao, Phase-transformation engineering in MoS_2 on carbon cloth as flexible binder-free anode for enhancing lithium storage, J. Alloys Compd. 716 (2017) 112–118.
[23] W. Yao, X. He, Z. Zheng, D. Liu, J. Song, Y. Zhu, Surface-modified composite separator for lithium-ion battery with enhanced durability and security, Prog. Nat. Sci. Mater. Int. 33 (6) (2024) 804–811.
[24] X. Han, X. Li, R. Chai, S. Wang, Y. Yuan, Y. Li, Trace Mg^{2+} doping enhances structural stability of single-crystal layered oxides for sodium-ion batteries, Prog. Nat. Sci. Mater. Int. 35 (3) (2025) 533–540.
[25] H. Ye, C. Zhang, Y. Li, W. Zhang, K. Zhang, B. Li, W. Hua, K. Wang, K. Xu, Advanced covalent-organic framework materials for sodium-ion battery, Prog. Nat. Sci. Mater. Int. 33 (6) (2024) 754–766.
[26] Y. He, C. Liu, Z. Xie, P. Xiaokaiti, G. Chen, Z. Feng, Y. Kasai, A. Abudula, G. Guan, Construction of cobalt sulfide/molybdenum disulfide heterostructure as the anode material for sodium ion batteries, Adv. Compos. Hybrid Mater. 6 (2023) 85.
[27] G. Zu, S. Xu, C. Wang, H. Li, M. Zhang, X. Ke, Y. Hu, R. Wang, J. Wang, Unraveling structure evolution failure mechanism in MoS_2 anode for improving lithium storage stability, J. Mater. Sci. Technol. 128 (2022) 245–253.
[28] Z. Lei, J. Zhan, L. Tang, Y. Zhang, Y. Wang, Recent development of metallic (1T) phase of molybdenum disulfide for energy conversion and storage, Adv. Energy Mater. 8 (19) (2018) 1703482.
[29] X. Geng, Y. Jiao, Y. Han, A. Mukhopadhyay, L. Yang, H. Zhu, Freestanding metallic 1T MoS_2 with dual ion diffusion paths as high rate anode for sodium-ion batteries, Adv. Funct. Mater. 27 (40) (2017) 1702998.
[30] X. Geng, Y. Jiao, Y. Han, A. Mukhopadhyay, L. Yang, H. Zhu, Batteries: freestanding metallic 1T MoS_2 with dual ion diffusion paths as high rate anode for sodium-ion batteries, Adv. Funct. Mater. 27 (40) (2017) 1702998.
[31] W. Li, H. Li, Z. Lu, L. Gan, L. Ke, T. Zhai, H. Zhou, Layered phosphorus-like GeP_5: a promising anode candidate with high initial coulombic efficiency and large capacity for lithium ion batteries, Energy Environ. Sci. 8 (2015) 3629–3636.
[32] J. Zhou, Q. Shi, S. Ullah, X. Yang, A. Bachmatiuk, R. Yang, M.H. Rummeli, Phosphorus-based composites as anode materials for advanced alkali metal ion batteries, Adv. Funct. Mater. 30 (49) (2020) 2004648.
[33] J. Zhang, K. Song, L. Mi, C. Liu, X. Feng, J. Zhang, W. Chen, C. Shen, Bimetal synergistic effect induced high reversibility of conversion-type Ni@$NiCo_2S_4$ as a free-standing anode for sodium ion batteries, J. Phys. Chem. Lett. 11 (4) (2020) 1435–1442.
[34] Y. Wan, K. Song, W. Chen, C. Qin, X. Zhang, J. Zhang, H. Dai, Z. Hu, P. Yan, C. Liu, S. Sun, S.L. Chou, C. Shen, Ultra-high initial coulombic efficiency induced by interface engineering enables rapid, stable sodium storage, Angew. Chem. Int. Ed. 60 (20) (2021) 11481–11486.
[35] S. Ma, J. Zhao, Q. Gao, C. Song, H. Xiao, F. Li, G. Li, Breaking mass transport limitations by iodized polyacrylonitrile anodes for extremely fast-charging lithium-ion batteries, Angew. Chem. Int. Ed. 62 (52) (2023) e202315564.
[36] C. Ma, D. Hou, J. Jiang, Y. Fan, X. Li, T. Li, Z. Ma, H. Ben, H. Xiong, Elucidating the synergic effect in nanoscale MoS_2/TiO_2 heterointerface for Na-Ion storage, Adv. Sci. 9 (35) (2022) 2204837.
[37] C. Ma, H. Li, Z. Li, G. Han, X. Tang, J. Qian, R. Chen, Atomic Co-Driven catalysis in MoS_2 for accelerated charge transfer and stable interfacial chemistry in sodium-ion batteries, Energy Storage Mater. 82 (2025) 104611.
[38] W. Zhao, M. Wang, H. Lin, K. Kim, R. He, S. Feng, H. Liu, Research progress on electrolyte key salts for sodium-ion batteries, Prog. Nat. Sci. Mater. Int. 34 (2) (2024) 263–273.
[39] X. Han, X. Li, R. Chai, S. Wang, Y. Yuan, Y. Li, Trace Mg^{2+} doping enhances structural stability of single-crystal layered oxides for sodium-ion batteries, Prog. Nat. Sci. Mater. Int. 35 (3) (2025) 533–540.